ACS APPLIED MATERIALS & INTERFACES

Functional Inorganic Materials and Devices

Electric Field Control of Magnetic Permeability in Co-fired Laminate Magnetoelectric Composites: A Phase-field Study for Voltage Tunable Inductor Applications

Liwei Geng, Yongke Yan, Shashank Priya, and Yu U. Wang

ACS Appl. Mater. Interfaces, **Just Accepted Manuscript** • DOI: 10.1021/acsami.0c12765 • Publication Date (Web): 11 Sep 2020

Electric Field Control of Magnetic Permeability in Co-fired Laminate Magnetoelectric Composites: A Phase-field Study for Voltage Tunable Inductor Applications

Liwei D. Geng,[1] Yongke Yan,[2] Shashank Priya,[2] and Yu U. Wang[1,*]

[1]Department of Materials Science and Engineering,
Michigan Technological University, Houghton, Michigan 49931, USA
[2]Department of Materials Science and Engineering,
Pennsylvania State University, University Park, Pennsylvania 16802, USA

ABSTRACT: Control of magnetic permeability through electric field in magnetoelectric materials promises to create novel voltage tunable inductors (VTIs). VTIs synthesized using co-fired ceramic processing exhibit many advantages over traditional epoxy bonding method, but the internal residual stress in co-fired VTIs resulting from thermal expansion mismatch hinders a full exploitation of the tunability of permeability. To find the optimal condition for high tunability of co-fired VTIs, domain-level phase field modeling and computer simulation are employed to study co-fired magnetoelectric composites comprising of NiZn ferrite and PZT. Two key factors important towards increasing the inductor tunability are systematically investigated, intrinsic magnetocrystalline anisotropy of the ferrite material and internal residual stress caused by the co-firing process. The simulations indicate that in order to achieve a large tunability, the tuned permeability should be confined within the linear region of the reciprocal of susceptibility and stress. Additionally, both magnetocrystalline anisotropy and residual stress should be as small as possible. These results provide a design strategy for realizing high-tunability co-fired VTIs.

KEYWORDS*: Phase field model; Magnetoelectric composite; Ferrite; Co-firing; Domain mechanism; Voltage tunable inductor*

---

* Author to whom correspondence should be addressed; electronic mail: wangyu@mtu.edu

1. INTRODUCTION

As one of fundamental passive components of electronic circuits, inductors find widespread use in various applications including filters, power converters, control electronics, communication systems, etc. In recent years, the laminate magnetoelectric (ME) composites made of magnetostrictive and piezoelectric materials with a 2-2 connectivity scheme have shown the control of magnetic permeability as a function of electric field or voltage. This control is provided by the ME coupling effect[1-5] that arises from the elastic coupling between magnetostrictive and piezoelectric properties. Tunability of magnetic permeability through electric field promises to develop a new class of electronic components, voltage tunable inductors (VTIs)[6-11], that will have transformative impact in the design of power electronics. In contrast to conventional tunable inductors, whose tunability is achieved by mechanically tuning bias magnets or electrically adjusting current in solenoids, VTIs provide on-chip integration capability, low power-consumption, higher tunability and smaller footprint, which is very important for enhancing the efficiency of power electronics as well as reducing the number of passives.

Recently, a VTI with colossal inductance tunability and low loss was proposed[12]. Utilizing the ME laminate composite fabricated via epoxy bonding of NiZn-ferrite/PMN-PT thin layers, the VTI was found to exhibit a remarkable high tunability of over 750% up to 10MHz, which completely covers the frequency range of state-of-the-art power electronics[12]. However, the fabrication of VTIs using epoxy bonding technique is not appealing for practical applications. Co-firing of VTIs is the most desirable processing method due to the strong interface stress coupling, easy miniaturization, and cost-effective mass production. More importantly, co-firing of VTIs is compatible with the current multilayer ceramic co-firing process. This process is currently being utilized by industry to manufacture low cost multilayer ceramic capacitor, multilayer piezoelectric actuator, and multilayer ferrite beads.

One potential challenge with co-fired VTIs is the large internal stress arising from the difference in thermal expansion coefficients of piezoelectric and magnetostrictive materials. This large residual stress exerted on the magnetostrictive layer will influence the inductance tunability. Figure 1(a) shows the inductance of a co-fired NiZn-ferrite/PMN-PT composite VTI under the tuning electric field[10]. In comparison with the epoxy bonded VTI, where the inductance or permeability is significantly decreased under the electric field with a large tunability as shown in Fig. 1(b), the co-fired VTI exhibits an increasing inductance and a small tunability (~20%). This difference in inductance behavior is attributed to the residual stress that is exerted on the ferrite layer at zero electric field, which can be illustrated schematically by Fig. 1(c). The general behavior of permeability and stress in Fig. 1(c) arises from the magnetization distribution and evolution mechanisms that are modulated by the stress-induced anisotropy[13]. It is the internal residual stress that determines the tuning regime of a VTI. For epoxy bonded VTIs, there is no residual stress under zero electric field and the tuning field results in a compressive stress on the ferrite layer and thus a decreased permeability. In the case of co-fired VTIs, there is an initial residual tensile stress that is reduced by the tuning field, leading to an increased permeability. It is worth noting that Fig. 1(c) is based on the negative magnetostriction coefficient of the magnetostrictive layer (NiZn-ferrite). Magnetostrictive materials with positive magnetostriction coefficient will exhibit opposite permeability-stress behavior to that shown in Fig. 1(c). The permeability behavior of epoxy bonded VTIs in the compressive stress regime has been systematically studied in our prior work[14], but the study for co-fired VTIs in the tensile stress regime is still lacking. The small tunability exhibited by the co-fired VTI in Fig. 1(a) needs to be investigated to identify the conditions under which the large tunability can be achieved.

In this study, co-fired NiZn-ferrite/PZT ME laminate composites are investigated by employing the domain-level phase field modeling and the computer simulation. Since there are two key factors for high tunability, namely, the intrinsic magnetocrystalline anisotropy (MCA) of the magnetostrictive material and the internal residual stress arising during the co-firing process, the main focus is on evaluating their role on the simulated magnetic permeability and tunability behaviors in this ME composite system. A theoretical analysis is presented in order to provide comprehensive understanding of the underlying mechanisms.

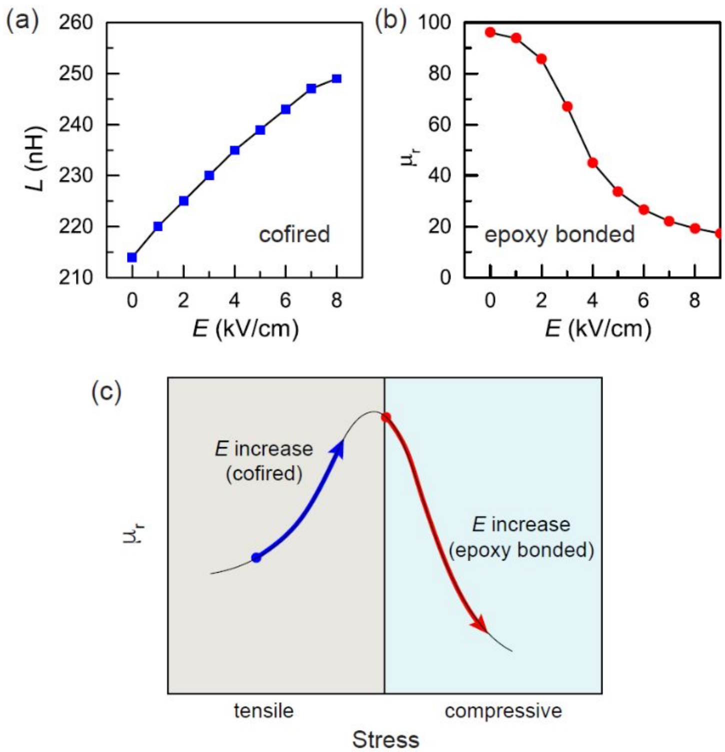

Figure 1. Measured inductance or permeability under electric field of VTIs fabricated through (a) co-firing and (b) epoxy bonding for NiZn-ferrite/PMN-PT ME composites. (c) Schematic illustration of permeability-stress behavior for these two cases, when the magnetostriction coefficient is negative for NiZn-ferrite material.

2. EXPERIMENTAL SECTION

To systematically study the effects of MCA and residual stress on the co-fired ferrite/PZT ME composite VTI system, we employed the domain-level phase field modeling and perform computer simulations. The phase field model of ME composites developed in our previous work[15] was adopted, which integrated the phase field models of magnetostrictive materials[16] and ferroelectric materials[17] into one unified model to treat domain processes and granular microstructures in polycrystalline composites of magnetostrictive and ferroelectric phases. This section will briefly describe this ME composite model, while more detailed description can be found elsewhere[14-15, 18].

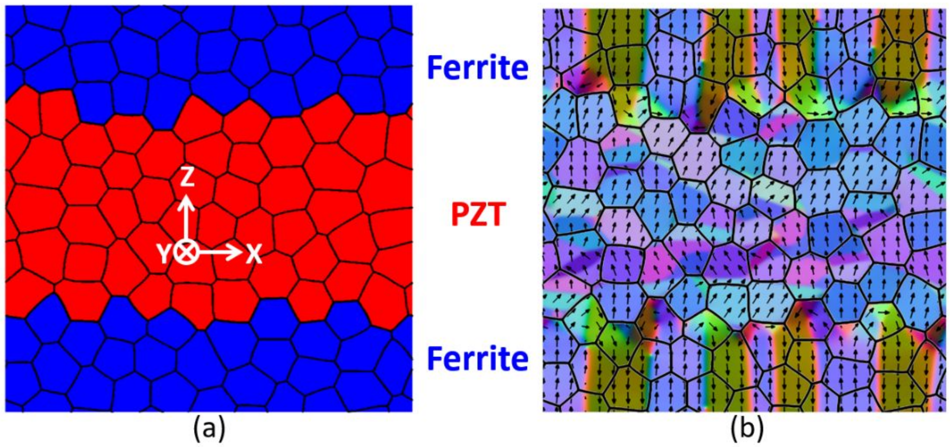

Figure 2. (a) Grain structure and phase morphology of ME composite. Blue color represents magnetostrictive ferrite phase and red color represents piezoelectric PZT phase. (b) Domain structure for both PZT layer and ferrite layer at E=0. Black arrows represent polarization or magnetization distribution. Color contours represent the three components of polarization or magnetization.

In this ME composite model, the system can be described by field variables of magnetization $\mathbf{M}(\mathbf{r})$, polarization $\mathbf{P}(\mathbf{r})$, and free charge density $\rho(\mathbf{r})$. The total system free energy under external magnetic field $\mathbf{H}^{ex}$ and electric field $\mathbf{E}^{ex}$ is given by[15]

$$F = \int\left[(1-\eta)f_M(R_{ij}M_j) + \eta f_E(R_{ij}P_j) + \beta_M|\nabla\mathbf{M}|^2 + \beta_E|\nabla\mathbf{P}|^2 - \mu_0\mathbf{H}^{ex}\cdot\mathbf{M} - \mathbf{E}^{ex}\cdot\mathbf{P}\right]d^3r \quad (1)$$
$$+\int\frac{d^3k}{(2\pi)^3}\left[\frac{\mu_0}{2}|\mathbf{n}\cdot\tilde{\mathbf{M}}|^2 + \frac{1}{2\varepsilon_0}\left|\frac{\tilde{\rho}}{k} - i\mathbf{n}\cdot\tilde{\mathbf{P}}\right|^2 + \frac{1}{2}K_{ijkl}\tilde{\varepsilon}_{ij}\tilde{\varepsilon}^*_{kl}\right]$$

where $f_M(R_{ij}M_j)$ and $f_E(R_{ij}P_j)$ respectively represent the local free energy density functions of magnetostrictive and ferroelectric phases. The operations $R_{ij}M_j$ and $R_{ij}P_j$ transform $\mathbf{M}(\mathbf{r})$ and $\mathbf{P}(\mathbf{r})$ from the global sample system to the local crystallographic system in each grain by means of the grain rotation matrix field $R_{ij}(\mathbf{r})$. The magnetostrictive phase (η=0) and ferroelectric phase (η=1) are distinguished by the phase field $\eta(\mathbf{r})$. The two-phase morphology of the ME composite is illustrated in Fig. 2(a). $f_M(\mathbf{M})$ represents the MCA energy of cubic symmetry in the local coordinate system[19]:

$$f_M(\mathbf{M}) = K_1\left(m_1^2m_2^2 + m_2^2m_3^2 + m_3^2m_1^2\right) \quad (2)$$

where $\mathbf{m}=\mathbf{M}/M$ is the magnetization direction and K_1 is the MCA constant. $f_E(\mathbf{P})$ is formulated by the Landau-Ginzburg-Devonshire (LGD) polynomial energy[20]:

$$\begin{aligned} f_{\mathrm{E}}(\mathbf{P}) &= \alpha_1\left(P_1^2+P_2^2+P_3^2\right)+\alpha_{11}\left(P_1^4+P_2^4+P_3^4\right)+\alpha_{12}\left(P_1^2P_2^2+P_2^2P_3^2+P_3^2P_1^2\right) \\ &+\alpha_{111}\left(P_1^6+P_2^6+P_3^6\right)+\alpha_{112}\left[P_1^4\left(P_2^2+P_3^2\right)+P_2^4\left(P_3^2+P_1^2\right)+P_3^4\left(P_1^2+P_2^2\right)\right] \\ &+\alpha_{123}P_1^2P_2^2P_3^2 \end{aligned} \tag{3}$$

The two gradient terms in Eq. (1) characterize the energy contributions from the magnetic exchange energy and polarization gradient, respectively. The **k**-space integral terms characterize the long-range magnetostatic, electrostatic and elastostatic interactions, where $K_{ijkl}=C_{ijkl}-n_mC_{ijmn}\Omega_{np}C_{klpq}n_q$, $\Omega_{ik}=(C_{ijkl}n_jn_l)^{-1}$. $\tilde{\mathbf{M}}$, $\tilde{\mathbf{P}}$, $\tilde{\rho}$ and $\tilde{\boldsymbol{\varepsilon}}$ in **k**-space are the corresponding Fourier transforms of the field variables **M**, **P**, ρ and ε in **r**-space. The spontaneous strain $\boldsymbol{\varepsilon}$ is responsible for the cross-linking between magnetization **M** and polarization **P** through the function of $\varepsilon_{ij}=\lambda_{ijkl}m_km_l+Q_{ijkl}P_kP_l$, where λ_{ijkl} and Q_{ijkl} are magnetostrictive and electrostrictive coefficient tensors, respectively.

The magnetization $\mathbf{M}(\mathbf{r},t)$ and polarization $\mathbf{P}(\mathbf{r},t)$ evolutions are respectively governed by the Landau-Lifshitz-Gilbert equation[19] and the time-dependent Ginzburg-Landau equation[20]:

$$\frac{\partial\mathbf{M}(\mathbf{r},t)}{\partial t}=\gamma\,\mathbf{M}\times\frac{\delta F}{\delta\mathbf{M}(\mathbf{r},t)}+\alpha\,\mathbf{M}\times\left[\mathbf{M}\times\frac{\delta F}{\delta\mathbf{M}(\mathbf{r},t)}\right] \tag{4}$$

$$\frac{\partial\mathbf{P}(\mathbf{r},t)}{\partial t}=-L\frac{\delta F}{\delta\mathbf{P}(\mathbf{r},t)} \tag{5}$$

while the evolution of free charge density field $\rho(\mathbf{r},t)$ is governed by continuity equation of electric charge as well as the microscopic Ohm's law[21]:

$$\frac{\partial\rho(\mathbf{r},t)}{\partial t}=-\nabla\cdot\mathbf{j}(\mathbf{r},t) \tag{6}$$

$$j_i=\sigma_{ik}E_k \tag{7}$$

where the local electric field $\mathbf{E}(\mathbf{r})$ is given by

$$\mathbf{E}(\mathbf{r})=\mathbf{E}^{ex}-\frac{1}{\varepsilon_0}\int\frac{d^3k}{(2\pi)^3}\left[\mathbf{n}\cdot\tilde{\mathbf{P}}(\mathbf{k})+i\frac{\tilde{\rho}(\mathbf{k})}{k}\right]\mathbf{n}e^{i\mathbf{k}\cdot\mathbf{r}}. \tag{8}$$

To systematically study the MCA and residual stress effects in co-fired ferrite/PZT ME composite system, varying MCA constant K_1 and thermal mismatch strain ε_{th} are considered in our simulations. Following material parameters are adopted in our simulations: MCA constant $K_1 \in [-15000, 15000]$ J/m^3, thermal mismatch strain $\varepsilon_{th} \in [-2.6, -6.6] \times 10^{-3}$, saturation magnetization $M_s = 3.5 \times 10^5$ A/m, saturation magnetostriction constant $\lambda_s = -18 \times 10^{-6}$ for the ferrite system; and LGD coefficients α_1=-2.67×10^7 m/F, α_{11}=-1.43×10^7 m^5/C^{2}F, α_{12}=1.57×10^7 m^5/C^{2}F, α_{111}=1.34×10^8 m^9/C^{4}F, α_{112}=1.17×10^9 m^9/C^{4}F, α_{123}=-4.77×10^9 m^9/C^{4}F, electrostrictive constants Q_{11}=0.0966 m^4/C^2, Q_{12}=-0.046 m^4/C^2, Q_{44}=0.0819 m^4/C^2 for $Pb(Zr_{0.5}Ti_{0.5})O_3$[20, 22]. Consideration of PZT instead of PMN-PT will not change the general behaviors of the ME composite VTIs. The layer thickness of PZT and ferrite in this ME composite system is approximately 4μm.

3. RESULTS AND DISCUSSION

3.1 Magnetocrystalline anisotropy effect

Magnetic anisotropy is crucial in determining the magnitude of permeability and tunability of a VTI system. This includes MCA, shape anisotropy, and stress-induced anisotropy. In a co-fired ME composite, the stress-induced anisotropy results from the internal residual stress and the external electric field. The electric field is applied on the piezoelectric layer to induce a stress on the magnetostrictive layer via strain-mediated ME coupling, which further results in a tunable permeability. The internal residual stress caused by the co-firing process is hard to be avoided. Its magnitude depends on temperature change, thermal expansion coefficients and layer thickness ratio. The shape anisotropy strongly depends on the shape geometry and the domain structure in the magnetostrictive layer. The intrinsic MCA can be effectively modified by doping a small fraction of Co^{2+} into ferrite materials[23]. Among the three anisotropies, the MCA and residual stress can significantly impact VTIs' permeability behaviors, and thus these two are key factors in governing the performance of a co-fired VTI system.

To examine the MCA effect, various magnitude of MCA constant K_1 in the range of -15000 to 15000 J/m^3 are considered in our simulations, while the thermal mismatch strain is fixed. It can be approximated that[24-27] the average thermal expansion coefficient is $\alpha_{PZT} \approx 7\,ppm$ for PZT, while for NiZn ferrite the value is $\alpha_{ferrite} \approx 11ppm$. Considering the ME composite with the same layer thickness for PZT and ferrite, as well as a temperature change from 930 °C to room temperature during the co-firing process, the residual thermal mismatch strain of $\varepsilon_{th} \approx -3.6\times10^{-3}$ is exerted on the PZT layer. This value is fixed in the analysis presented in this section.

To obtain the magnetic permeability as well as the corresponding tunability for each K_1, the same simulation procedure is followed in all cases. First, co-fired ferrite/PZT composite with residual thermal mismatch strain and poled PZT layer is implemented. To do so, an additional mismatch strain $\varepsilon_{ii}^{0} = -3.6\times10^{-3}$ is introduced to the PZT layer in the phase field modeling. Such a large in-plane (XY-plane) compressive strain will be partially canceled by the poling process of the PZT layer. So, there is a residual tensile stress exerted on the ferrite layer, which gives rise to a positive stress-induced uniaxial anisotropy K_σ along Z-axis (due to the negative magnetostriction) and thus a stripe domain structure. Figure 2(b) shows the domain structure for PZT and ferrite layers under zero electric field. As expected, polarizations are well orientated in Z-axis (poling direction), while magnetizations form a stripe domain structure due to the stress-induced uniaxial anisotropy. Second, a tuning electric field of given magnitude along Z-axis is applied on the PZT layer, which will induce an additional stress on the ferrite layer due to strain-mediated ME coupling. Third, after both polarizations and magnetizations reach equilibrium, a small magnetic field ΔH is applied along X-axis to induce a small magnetization response ΔM along X-axis, and then the magnetic permeability for this ME composite at tuning electric field is obtained by $\mu = \chi + 1 = \Delta M / \Delta H + 1$.

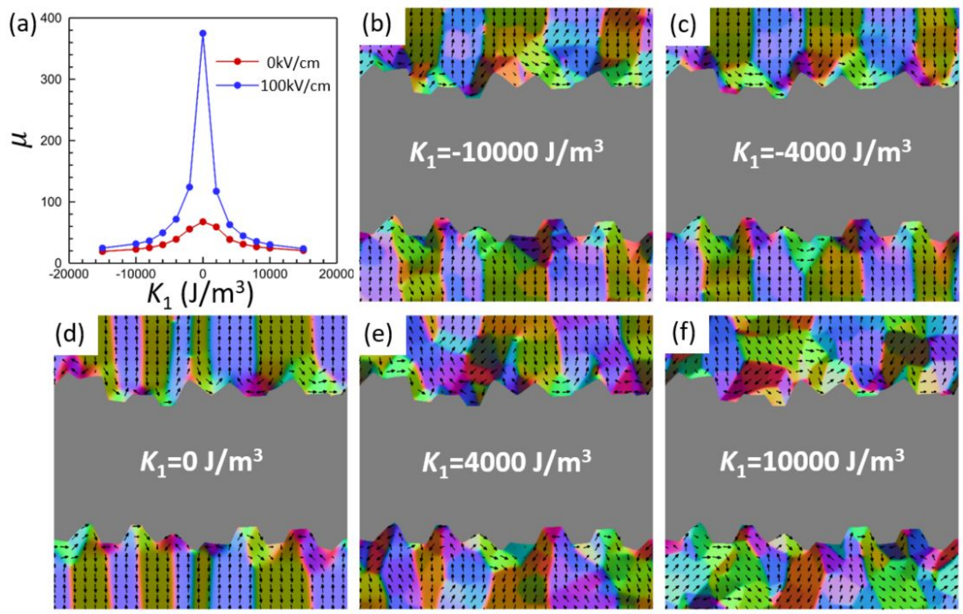

Figure 3. (a) Magnetic permeability μ with various MCA constant K_1 at E=0 and 100 kV/cm. Magnetic domain structures of ferrite layer at E=0 kV/cm with (b) K_1= -10000 J/m^3, (c) K_1= -4000 J/m^3, (d) K_1= 0 J/m^3, (e) K_1= 4000 J/m^3, and (f) K_1= 10000 J/m^3. Black arrows represent magnetization distribution. Color contours represent the three components of magnetization.

Following the above simulation procedure, the initial permeability determined at electric field E=0 kV/cm with varying K_1 is shown in Fig. 3(a), and the corresponding magnetic domain structures are shown in Fig. 3(b)-(f). It is noted that smaller magnitude of MCA constant K_1 results in larger permeability and K_1=0 corresponds to the largest permeability, which can be explained by the domain rotation mechanism. Lower MCA makes magnetizations rotate more easily under magnetic field and thus results in a larger magnetization response ΔM and hence a larger permeability μ. On the contrary, higher MCA energy will suppress the magnetization rotation and result in a smaller permeability. It is also noted that the permeability at E=0 kV/cm is very low even at K_1=0 (μ=67), which is attributed to the residual stress-induced anisotropy caused by the thermal mismatch strain during the co-firing process. Such a positive stress-induced uniaxial anisotropy prefers to align magnetizations along Z-axis to form a stripe domain structure; therefore, when the stress-induced anisotropy dominates, a stripe domain structure is formed, as shown in Fig. 3. Even for the same $|K_1|$, the domain structures could be different. One can notice that the domain structure with negative K_1 is more striped than that with positive K_1 for the same magnitude of $|K_1|$. According to Eq. (2), since the energy barrier between the easy axes for negative K_1 is lower than that for positive K_1, the magnetization rotation is easier and thus the domain structure is more striped for negative K_1.

In this ME composite VTI system, the tuning electric field applied to the PZT layer along Z-axis exerts a compressive stress on the ferrite layer via the ME coupling, which eventually results in a tunable permeability. Electric field control of magnetic permeability behaviors for the ME composite with various MCA constant K_1 has been simulated, but herein, we only show three representatives cases in detail: one for pure NiZn ferrite (K_1= -6000 J/m^3, Fig. 6) and two for Co-modified NiZn ferrite with reduced (K_1= -2000 J/m^3, Fig. 5) and eliminated (K_1= 0 J/m^3, Fig. 4) MCA. Analysis of these three cases can help us in better understanding of the underlying domain-level mechanisms influenced by the MCA effect.

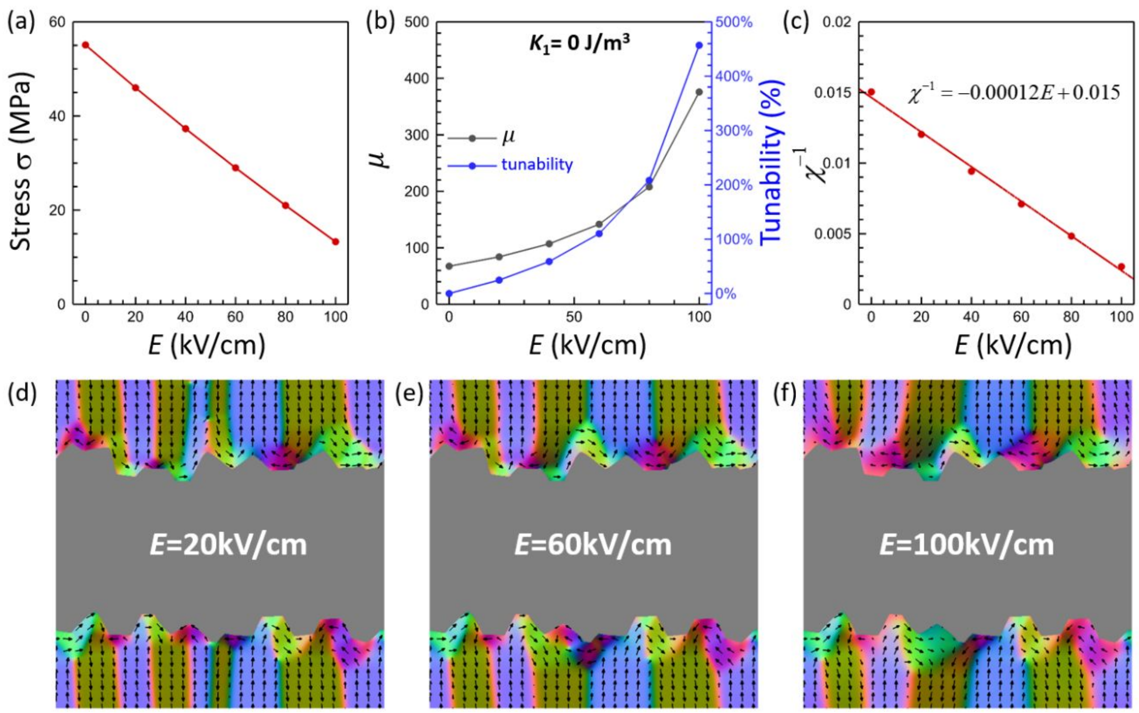

Figure 4. (a) The in-plane tensile stress σ on ferrite layer induced by electric field E. (b) Magnetic permeability μ and tunability $\gamma = (\mu_E - \mu_0)/\mu_0$ as a function of electric field E for VTI with K_1= 0 J/m^3. (c) Linear fitting of χ^{-1} with electric field E. The corresponding magnetic domain structures of ferrite layer under (d) E=20 kV/cm, (e) E=60 kV/cm, and (f) E=100 kV/cm.

Figure 4 shows the simulated results of the VTI with K_1= 0 J/m^3. Starting from the initial domain structure shown in Fig. 3(d), tuning electric field up to 100kV/cm is applied. The induced in-plane stress on the ferrite layer under electric field is shown in Fig. 4(a). The initial in-plane residual (tensile) stress is 55MPa at E=0 kV/cm, resulting from the residual thermal mismatch strain ε_{th} that is partially canceled by the poling-process strain ε_p. Such a residual stress is weakened by the increasing electric field, exhibiting a nearly linear relationship between σ and E. Since PZT considered in the simulation has a smaller d_{31} than PMN-PT in the experiment, higher electric field is needed in the simulation to produce the same tunable stress as in the experiment. Actually, the electric field E=100 kV/cm in simulations is roughly equivalent to E=10 kV/cm in experiments (Fig. 1), while both of them produce the same tuning range of stress, ~40 MPa. It is worth noting that the σ~E relation in Fig. 4(a) also applies to other cases in this section because of the same residual stress.

As the electric field increased, the magnetic permeability μ and the corresponding tunability defined by $\gamma = (\mu_E - \mu_0)/\mu_0$ are also increased, as shown in Fig. 4(b). Since the MCA is eliminated, the stress-induced anisotropy K_σ dominates, which results in stripe domains as illustrated in Fig. 3(d) and Fig. 4(d)-(f) with electric field values of E=0, 20, 60, 100 kV/cm, respectively. Electric field reduces the in-plane tensile stress or K_σ, and therefore, the permeability is increased. When the electric field is as high as 100 kV/cm, the tensile stress becomes very low (13 MPa), resulting in a large permeability ($\mu = 376$) as well as a high tunability ($\gamma \approx 500\%$), as shown in Fig. 4(b). Smaller stress-induced anisotropy usually results in larger domain size and hence a weaker stripe domain structure, as illustrated in Fig. 4(e)-(f). Further, the stripe domain structure also indicates that the permeability is mainly contributed by the domain rotation mechanism rather than the domain wall motion mechanism, which gives rise to a common linear relationship between χ^{-1} and E (or σ), as shown in Fig. 4(c), where the linear fitting gives $\chi^{-1} = -0.00012E + 0.015$. In fact, such a linearity commonly exists in many inductor systems[10, 13, 28], while the detailed analysis for this characteristic will be discussed in Sec. 3.2.

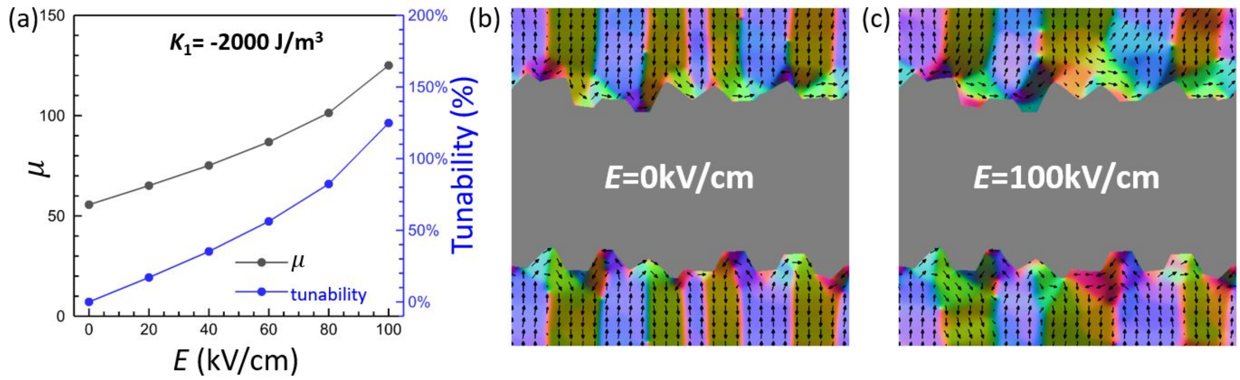

Figure 5. (a) Magnetic permeability μ and tunability $\gamma=(\mu_E-\mu_0)/\mu_0$ as a function of electric field E for VTI with K_1= -2000 J/m^3. The corresponding magnetic domain structures of ferrite layer under (b) E=0 kV/cm and (c) E=100 kV/cm.

For the VTI with K_1= -2000 J/m^3 (Fig. 5), the general behavior is quite similar, but the magnitude of magnetic permeability and its tunability is reduced. According to Fig. 5(a), the permeability is increased from $\mu=55$ to 125 under the electric field increase from E=0 to 100 kV/cm, corresponding to a tunability of 125%. Such a reduction is attributed to the larger MCA, since the stress-induced anisotropy under the same electric field is the same for both cases. Magnetic stripe domain structures under electric field E=0 and 100 kV/cm are illustrated in Fig. 5(b) and (c), respectively.

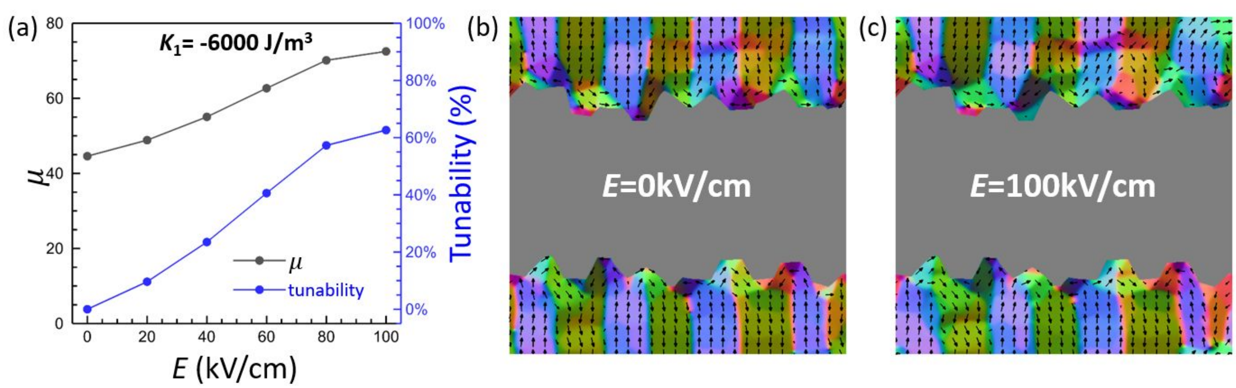

Figure 6. (a) Magnetic permeability μ and tunability $\gamma=(\mu_E-\mu_0)/\mu_0$ as a function of electric field E for VTI with K_1= -6000 J/m^3. The corresponding magnetic domain structures of ferrite layer under (b) E=0 kV/cm and (c) E=100 kV/cm.

Figure 6 shows the simulated results for the VTI with K_1= -6000 J/m^3, which represents the unmodified NiZn ferrite as mentioned above. The general behavior is similar to the above two cases in Fig. 4 and 5, although the magnitude of permeability and tunability is further reduced due to the larger MCA. According to Fig. 6(a), the permeability is increased from $\mu = 45$ to 73 under the electric field increase from E=0 to 100 kV/cm, corresponding to a tunability of 62%. When E>80 kV/cm, the permeability does not increase as fast as in the previous two cases; instead, a plateau appears with further increase in electric field. In fact, such a behavior is due to the reduced K_σ that becomes too weak to compete with the intrinsic MCA to maintain the stripe domain structure. As shown in Fig. 6(c), magnetizations begin to deviate from Z-axis, and one can expect that the critical electric field at which the stripe domain structure is destroyed should be larger than 100 kV/cm.

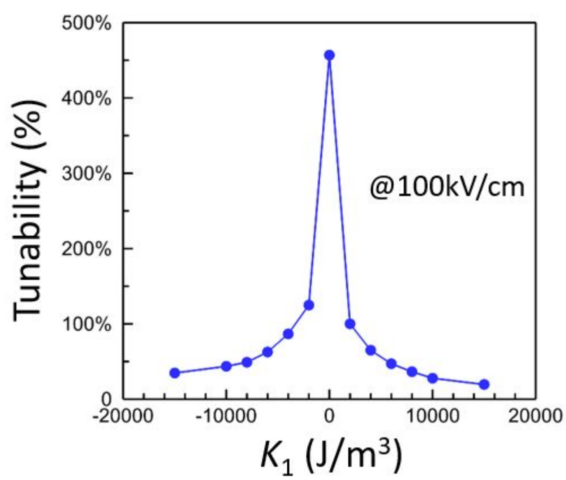

Figure 7. Tunability of magnetic permeability at E=100 kV/cm as a function of MCA constant K_1 for the co-fired ferrite/PZT ME composite VTI system.

The permeability tuned by electric field for all the cases are simulated in the same way as in Fig. 4-6. In particular, the simulated permeability at E=100 kV/cm for each MCA constant K_1 is plotted in Fig. 3(a). As shown in Fig. 3(a), both curves share the same tendency, but the permeability at E=100 kV/cm is always larger than that at E=0 kV/cm, which is attributed to the reduced stress-induced anisotropy at finite electric field. The corresponding tunability of permeability at E=100 kV/cm as a function of K_1 is plotted in Fig. 7. As shown in this figure, larger MCA results in a lower tunability while smaller MCA results in a higher tunability, and zero MCA corresponds to the highest tunability (~500%). This behavior is similar to that shown in Fig. 3(a). We know that the permeability is determined by the intrinsic MCA and the stress-induced anisotropy, while the tunability is realized by tuning the electric field (i.e., the stress-induced anisotropy). As such, large tunability can be achieved by enhancing the influence of electric field through reduction in the MCA (by means of alloying NiZn ferrite with a proper composition of Co ferrite), which briefly explains the simulated results in Fig. 7. Detailed analysis on this observation can be found in Sec. 3.2.

3.2 Residual stress effect

As discussed in Sec. 3.1, the thermal mismatch strain that arises from different thermal expansion coefficients of magnetostrictive and piezoelectric materials depends on the temperature change during the co-firing process as well as the layer thickness ratio, which indicates a possible means to engineer the residual stress. To systematically study the residual stress effect, thermal mismatch strain in a large range, $\varepsilon_{th} \in [-2.6, -6.6] \times 10^{-3}$, will be considered. The thermal mismatch strain of a given magnitude can exert a specific internal residual stress on the ferrite layer to modulate the permeability and tunability behaviors of VTIs. Based on our simulations results, there is a linear relationship between residual stress σ and thermal mismatch strain ε_{th}, as shown in Fig. 8(a). In particular, when $\varepsilon_{th} = -2.6 \times 10^{-3}$, it will be canceled by the additional strain resulting from the poling process ($\varepsilon_p = -2.6 \times 10^{-3}$), so that the residual stress is reduced to zero. Therefore, the corresponding residual tensile stress is $\sigma \in [0, 223]$ MPa, as shown in Fig. 8(a). To examine the residual stress effect, three representative values of MCA constant are considered, K_1= 0, -2000 and -6000 J/m^3.

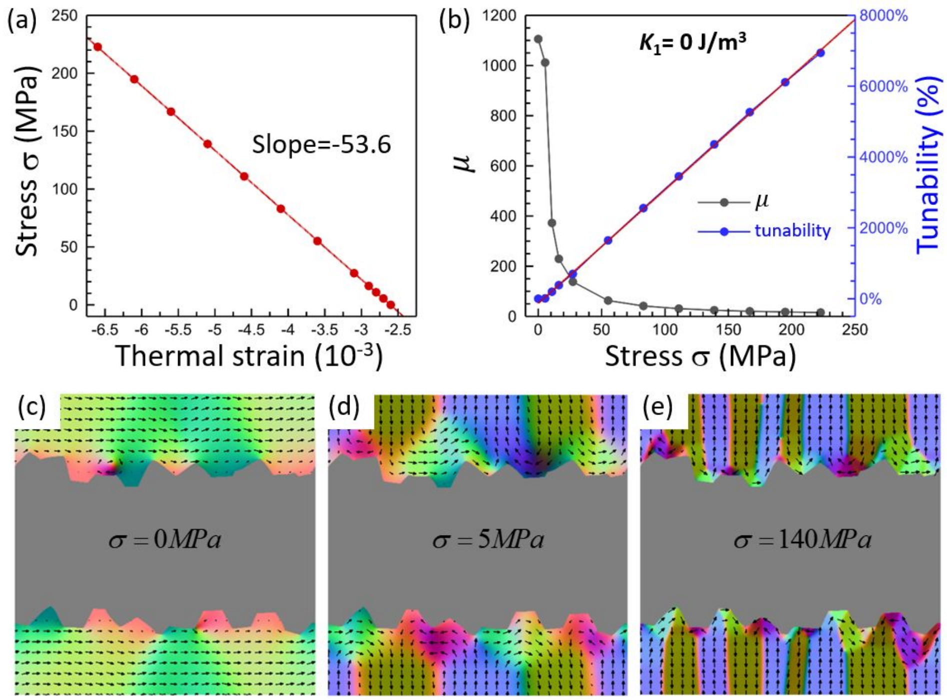

Figure 8. (a) Linear fitting of internal residual stress σ with thermal mismatch strain ε_{th}. (b) Magnetic permeability μ and tunability $\gamma = (\mu_0 - \mu_\sigma)/\mu_\sigma$ as a function of σ for VTI with MCA constant K_1= 0 J/m^3. The corresponding magnetic domain structures for ferrite layer under (c) $\sigma = 0MPa$, (d) $\sigma = 5MPa$, and (e) $\sigma = 140MPa$.

For the VTI with K_1= 0 J/m^3, the permeability changes from ~1100 to 16 under the residual stress up to 223MPa, which corresponds to a tunability up to ~7000% if it is defined by $\gamma = (\mu_0 - \mu_\sigma)/\mu_\sigma$, as shown in Fig. 8(b). The initial magnetic domain structure under zero residual stress is shown in Fig. 8(c), where the strong stray field from the ME interface results in an almost in-plane alignment of magnetizations. As the residual stress increases, a stripe domain structure is formed due to the stress-induced uniaxial anisotropy, as shown in Fig. 8(d) and (e). Larger residual stress usually results in a reduced exchange length and thus a smaller domain size. As mentioned in Sec. 3.1, the stripe domain structure indicates that the permeability is mainly attributed to the domain rotation process and hence a linear relationship between χ^{-1} and σ exists. Such a linearity is shown in Fig. 8(b) except the origin point at which the stripe domain structure is absent. It is worth noting that the permeability behavior tuned by electric field (13~55 MPa for E up to 100 kV/cm) in Fig. 4(b) is consistent with Fig. 8(b) with the same stress range. One can expect that a thermal mismatch strain that is slightly smaller than -3.6×10^{-3} can further increase the tunability in the same tuning range of electric field for this ME composite VTI system.

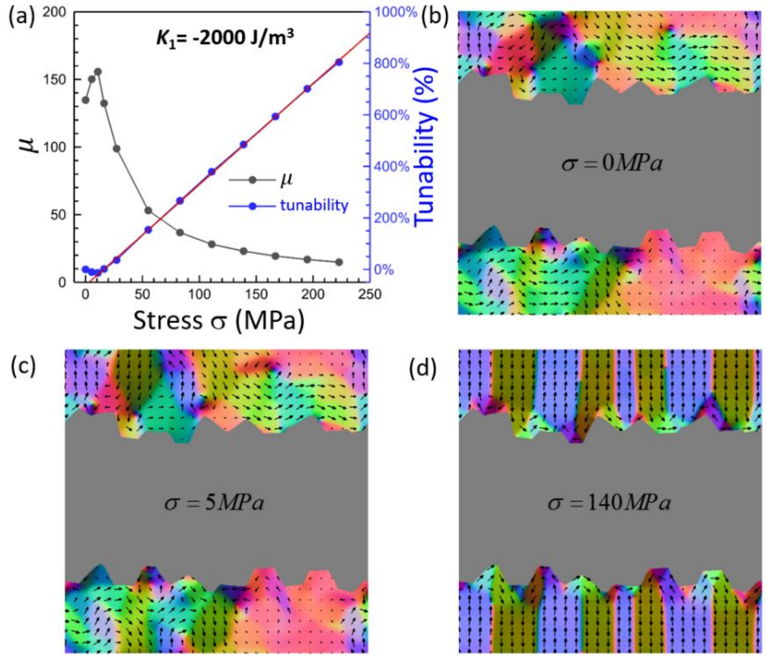

Figure 9. (a) Magnetic permeability μ and tunability $\gamma=(\mu_0-\mu_\sigma)/\mu_\sigma$ as a function of σ for VTI with MCA constant K_1= -2000 J/m^3. The corresponding magnetic domain structures for ferrite layer under (b) $\sigma=0MPa$, (c) $\sigma=5MPa$, and (d) $\sigma=140MPa$.

Figure 9 shows the simulated results for the VTI with K_1= -2000 J/m^3. The permeability changes from ~150 to 15 with increasing residual stress up to 223 MPa, which corresponds to a tunability up to ~800%, as shown in Fig. 9(a). As expected, the permeability magnitude is reduced in comparison with Fig. 8(b), because of the finite MCA. In addition, a small μ-peak emerges at small tensile stress ~10 MPa, which is absent in Fig. 8(b). In fact, when the residual stress is small, the stress-induced uniaxial anisotropy is not strong enough to compete with the intrinsic MCA. Once it exceeds a critical value, the stripe domain structure is formed. At the critical point, the domain rotation process occurs rapidly and thus the permeability could be very large, which gives rise to the μ-peak. Similar behavior is also observed in prior work on Terfenol-D/PZT ME composite system where a large μ-peak emerges due to the domain structure transition[13]. The linearity between tunability and stress is also observed when $\sigma>10MPa$. Similar to the case of

K_1= 0 J/m^3, the permeability behavior tuned by electric field in Fig. 5(a) is also consistent with Fig. 9(a) with the same stress range.

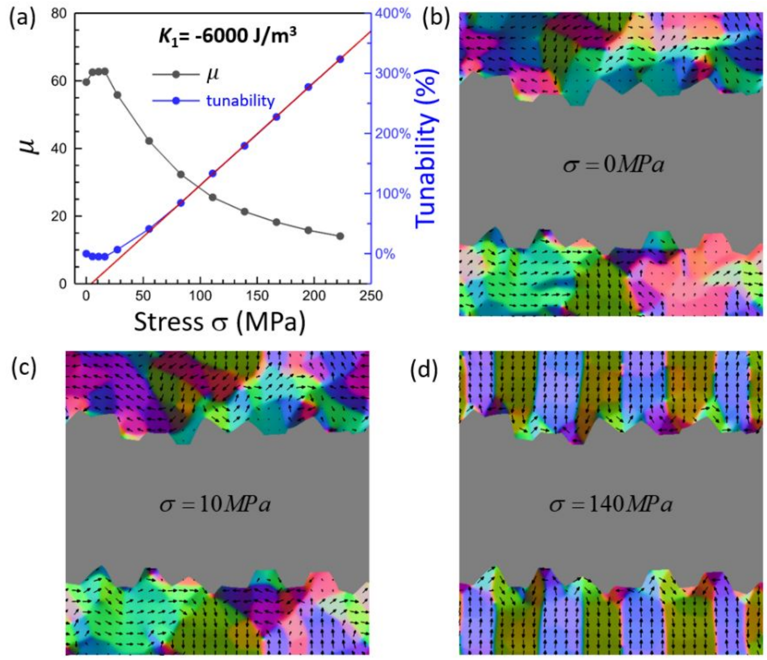

Figure 10. (a) Magnetic permeability μ and tunability $\gamma = (\mu_0 - \mu_\sigma) / \mu_\sigma$ as a function of σ for VTI with MCA constant K_1= -6000 J/m^3. The corresponding magnetic domain structures for ferrite layer under (b) $\sigma = 0MPa$, (c) $\sigma = 10MPa$, and (d) $\sigma = 140MPa$.

For the VTI with K_1= -6000 J/m^3, which corresponds to the pure NiZn ferrite, the permeability changes from ~60 to 14 under the bias tensile stress up to 223 MPa, which corresponds to a tunability up to ~300%, as shown in Fig. 10(a). Because of the larger MCA, the permeability is further reduced, and the small μ-peak is also slightly shifted toward a higher stress so that the linearity of $\gamma \sim \sigma$ appears when $\sigma > 50MPa$. The existence of the μ-peak explains the permeability behavior tuned by electric field at E>80 kV/cm in Fig. 6(a). In fact, such a permeability behavior shown in Fig. 9(a) and Fig. 10(a) commonly exists in ferrite materials with negative magnetostriction coefficient [29].

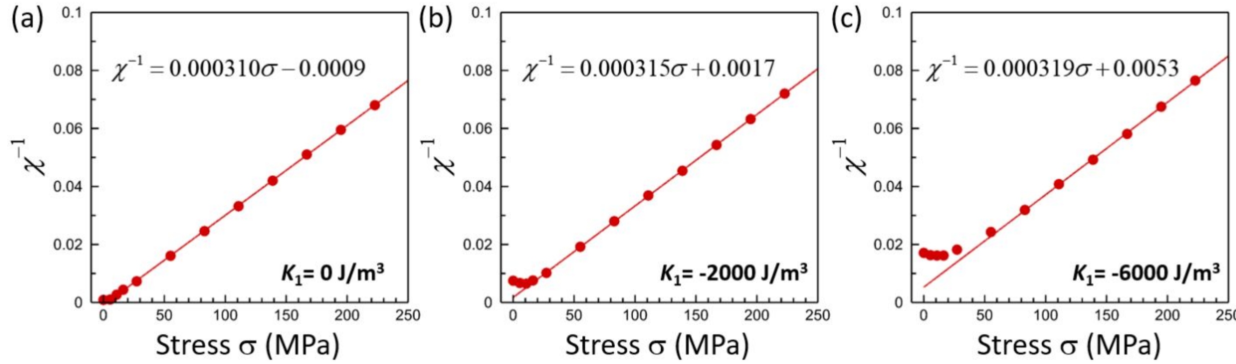

Figure 11. Linear fitting of χ^{-1} with residual stress σ for VTI with MCA constant (a) K_1= 0 J/m^3, (b) K_1= -2000 J/m^3, and (c) K_1= -6000 J/m^3.

To better understand the MCA effect and the residual stress effect on this co-fired ME composite VTI system, a theoretical analysis regarding the linear behavior between χ^{-1} and σ is presented as follows. According to the theoretical model developed for polycrystal laminate ME composites[13], the relationship between χ and σ can be described as:

$$\chi = \frac{K_d}{K_\sigma + K_0 - K_{dz}}, \tag{9}$$

where $K_d = \mu_0 M_s^2/2$, $K_\sigma = -3\lambda_s\sigma/2$ is the stress-induced uniaxial anisotropy, K_0 is the effective MCA, and K_{dz} is the demagnetization energy in Z-axis. Based on the theoretical model[13], K_0 is related to the intrinsic MCA constant K_1, and usually larger magnitude of K_1 results in a larger K_0, and $K_1 = 0$ corresponds to $K_0 = 0$. The demagnetization energy K_{dz} is determined by the shape geometry as well as the magnetic domain structure of the ferrite layer. The formation of a stripe domain structure, where the stray field of opposite directions cancels each other, significantly reduces the demagnetization energy K_{dz}. Therefore, one can predict that a smaller domain width can result in a smaller demagnetization energy K_{dz} for the ferrite layer with stripe domains. Since there is no big change in the stripe domain width based on our simulations, the demagnetization energy K_{dz} is assumed constant. According to Eq. (9), the susceptibility χ or permeability μ is dependent on the stress-induced anisotropy K_σ and the effective MCA K_0. For the same MCA, external electric field can decrease the tensile stress and the stress-induced anisotropy K_σ, so that the permeability is increased, as shown in Fig. 4(b), Fig. 5(a) and Fig. 6(a). For the same K_σ (or E), larger MCA can result in a smaller permeability, as shown in Fig. 3(a).

Eq. (9) can be also expressed by its reciprocal form given by

$$\chi^{-1} = \frac{K_\sigma + K_0 - K_{dz}}{K_d} = \frac{-3\lambda_s}{\mu_0 M_s^2}\sigma + \frac{2K_0}{\mu_0 M_s^2} - \frac{2K_{dz}}{\mu_0 M_s^2}, \tag{10}$$

which clearly demonstrates the linear behavior between χ^{-1} and σ, with the slope $-3\lambda_s / \mu_0 M_s^2$ and intercept $2(K_0 - K_{dz}) / \mu_0 M_s^2$. Considering the material parameters $\lambda_s = -18\times10^{-6}$ and $M_s = 3.5\times10^5\ A/m$ adopted in our simulations, the calculated slope is 0.00035 /MPa. The linear fittings of χ^{-1} vs. σ for the cases of K_1= 0, -2000, -6000 J/m^3 are shown in Fig. 11(a)-(c), respectively. It is noted that all the three fitted slopes (0.000310, 0.000315, 0.000319) are very close but slightly smaller than the theoretically calculated value of 0.00035. The theoretical value is based on the rigid stripe domain structure where all magnetizations are exactly aligned out of plane (Z-axis), while strong stray field generated from the ME interface makes the magnetizations near the interface align parallel with the interface, which reduces the susceptibility and thus leads to a smaller slope. As expected, the fitted intercepts increase with the MCA, which is also consistent with our theoretical analysis. Particularly, for eliminated MCA (K_1= 0 J/m^3), the fitted intercept is $-2K_{dz} / \mu_0 M_s^2 = -0.0009$, which corresponds to a small demagnetization energy $K_{dz} = 69$ J/m^3 that is much smaller than the ideal value $K_d = 7.7\times10^4$ J/m^3 determined only by the shape geometry. This indicates that a stripe domain structure can significantly reduce the demagnetization energy.

In order to achieve a high tunability, the tuned permeability cannot exceed the μ-peak, i.e., the allowed permeability falls into the linear region formulated by Eq. (9) and (10). Considering the linear relationship between χ^{-1} and σ, the tunability within a given range of electric field ΔE becomes

$$\gamma = \frac{\mu_{\sigma0-\Delta\sigma} - \mu_{\sigma0}}{\mu_{\sigma0}} \approx \frac{\chi_{\Delta\sigma}}{\chi} = \frac{K_{\Delta\sigma}}{K_{\sigma0} - K_{\Delta\sigma} + K_0 - K_{dz}}, \tag{11}$$

where $K_{\sigma 0}$ is the residual stress-induced anisotropy caused by the co-firing process, $\Delta\sigma$ is the tensile stress range induced by the tuning electric field ΔE, and $K_{\Delta\sigma}$ represents the corresponding anisotropy change resulted from $\Delta\sigma$. Eq. (11) indicates that within the same tuning range of electric field ΔE (i.e., $\Delta\sigma$ and $K_{\Delta\sigma}$ are fixed), large tunability prefers small $K_{\sigma 0}$ and K_0, i.e., smaller MCA and smaller residual stress can result in a larger tunability within the linear region of $\chi^{-1} \sim \sigma$. Therefore, based on our simulated results in Sec. 3.1, to achieve the highest tunability, zero MCA as well as an appropriate thermal mismatch strain that is slightly smaller than -3.6×10^{-3} is required.

The intrinsic MCA can be effectively modified by doping a small fraction of Co^{2+} into ferrite materials, i.e., alloying NiZn ferrite with a small composition of Co ferrite. As indicated by our previous work[12], adding 2% Co ferrite almost eliminates MCA while slightly increasing the magnetostrictive coefficient. Besides, an alternate way to modulate MCA is by modifying the composition of Zn. The residual stress in co-fired VTIs originates from three stages: (1) shrinkage mismatch during the sintering (heating); (2) thermal expansion mismatch after the sintering (cooling); and (3) piezoelectric stress during the electrical poling. The shrinkage mismatch can be tuned by controlling the initial grain density of ferrite and piezoelectric ceramic tapes via changing the binder content as well as the shrinkage rate via adding sintering aids. The thermal expansion mismatch can be tuned by modifying the material composition to adjust the expansion coefficient, or by adding another phase to compensate the thermal expansion difference between the two layers. The piezoelectric stress can be tuned by controlling the ferroelectric phase or grain orientation of the piezoelectric layer. Besides, the magnitude of residual stress can be further modified by adjusting the thickness ratio between magnetostrictive and piezoelectric layers. While this simulation work is on NiZn ferrite, the general conclusions can be also applied to other power ferrites like MnZn ferrite. However, since the magnetostrictive coefficient of MnZn ferrite is very small, the tunability of VTI utilizing MnZn ferrite is much smaller than NiZn ferrite under the same electric field.

4. CONCLUSION

In order to develop a fundamental design strategy for a large tunability in the co-fired laminate ME composite VTI system, we performed phase field simulations to systematically study the magnetic permeability behavior controlled by external electric field for the co-fired ferrite/PZT ME composites at the domain level. Two key factors responsible for VTIs' permeability and tunability behaviors were considered, namely, the intrinsic MCA of the ferrite material and the internal residual stress caused by the co-firing process. The intrinsic MCA of NiZn ferrite can be effectively modified by doping with small fraction of Co^{2+}. The residual stress arising in the co-fired ceramic composites due to mismatch of the thermal expansion coefficients between the ferrite and PZT phases is dependent of temperature change in the co-firing process as well as the layer thickness ratio. For the MCA effect, the permeability behaviors tuned by external electric field in VTIs with various MCA constant K_1 were studied. The simulation reveals that a larger permeability and tunability requires a smaller MCA. For the residual stress effect, a large range of thermal mismatch strain or residual stress is considered, and our simulations reveal a linear relationship between χ^{-1} and σ, which is attributed to the stripe domain structure formed in the ferrite layer resulted from the stress-induced uniaxial anisotropy. Such a linear relation is analyzed theoretically. The analysis indicates that in order to achieve a large tunability, the tuned permeability should avoid the μ-peak and fall into the linear region of $\chi^{-1} \sim \sigma$, and both the MCA and residual stress should be as small as possible. These findings provide a universal strategy to design high-tunability co-fired ME composite VTIs by means of modulation of MCA and residual stress.

ACKNOWLEDGMENTS

Financial support from DARPA MATRIX TE3 Program is acknowledged. The parallel computer simulations were performed on XSEDE supercomputers. S.P. acknowledges the financial support from National Science Foundation through award number 1904811.

REFERENCES

(1) Nan, C.-W. Magnetoelectric Effect in Composites of Piezoelectric and Piezomagnetic Phases. *Phys. Rev. B* **1994**, 50, 6082-6088.

(2) Nan, C.-W.; Bichurin, M. I.; Dong, S.; Viehland, D.; Srinivasan, G. Multiferroic Magnetoelectric Composites: Historical Perspective, Status, and Future Directions. *J. Appl. Phys.* **2008**, 103, 031101-031135.
(3) Ma, J.; Hu, J.; Li, Z.; Nan, C.-W. Recent Progress in Multiferroic Magnetoelectric Composites: from Bulk to Thin Films. *Adv. Mater.* **2011**, 23, 1062.
(4) Wang, Y.; Gray, D.; Berry, D.; Gao, J.; Li, M.; Li, J.; Viehland, D. An Extremely Low Equivalent Magnetic Noise Magnetoelectric Sensor. *Adv. Mater.* **2011**, 23, 4111.
(5) Sun, N. X.; Srinivasan, G. Voltage Control of Magnetism in Multiferroic Heterostructures and Devices. *SPIN* **2012**, 02, 1240004-1240049.
(6) Lou, J.; Reed, D.; Liu, M.; Sun, N. X. Electrostatically Tunable Magnetoelectric Inductors with Large Inductance Tunability. *Appl. Phys. Lett.* **2009**, 94, 112508-112510.
(7) Liu, G.; Cui, X.; Dong, S. A Tunable Ring-Type Magnetoelectric Inductor. *J. Appl. Phys.* **2010**, 108, 094106-094109.
(8) Lin, H.; Lou, J.; Gao, Y.; Hasegawa, R.; Liu, M.; Howe, B.; Jones, J.; Brown, G.; Sun, N. X. Voltage Tunable Magnetoelectric Inductors With Improved Operational Frequency and Quality Factor for Power Electronics. *IEEE Trans. Magn.* **2015**, 51, 4002705-4002709.
(9) Peng, B.; Zhang, C.; Yan, Y.; Liu, M. Voltage-Impulse-Induced Nonvolatile Control of Inductance in Tunable Magnetoelectric Inductors. *Phys. Rev. Appl.* **2017**, 7, 044015-044021.
(10) Yan, Y.; Geng, L. D.; Zhang, L.; Gao, X.; Gollapudi, S.; Song, H.-C.; Dong, S.; Sanghadasa, M.; Ngo, K.; Wang, Y. U.; Priya, S. Correlation Between Tunability and Anisotropy in Magnetoelectric Voltage Tunable Inductor (VTI). *Sci. Rep.* **2017**, 7, 16008-16017.
(11) Yan, Y.; Geng, L. D.; Zhang, L.; Tu, C.; Ramdas, R. M. S.; Liu, H.; Li, X.; Sanghadasa, M.; Ngo, K. D.; Wang, Y. U.; Priya, S. High Power Magnetoelectric Voltage Tunable Inductors. *IEEE Trans. Ind. Electron.* **2020**, doi:10.1109/tie.2020.2989719.
(12) Yan, Y.; Geng, L. D.; Tan, Y.; Ma, J.; Zhang, L.; Sanghadasa, M.; Ngo, K.; Ghosh, A. W.; Wang, Y. U.; Priya, S. Colossal Tunability in High Frequency Magnetoelectric Voltage Tunable Inductors. *Nat. Commun.* **2018**, 9, 4998-5005.
(13) Geng, L. D.; Yan, Y.; Priya, S.; Wang, Y. U. Electric Field Control of Magnetic Susceptibility in Laminate Magnetostrictive/Piezoelectric Composites: Phase-Field Simulation and Theoretical Model. *Phys. Rev. B* **2020**, 101, 054422-054432.
(14) Geng, L. D.; Yan, Y.; Priya, S.; Wang, Y. U. Computational Study of Cobalt-Modified Nickel-Ferrite/PZT Magnetoelectric Composites for Voltage Tunable Inductor Applications. *Acta Mater.* **2019**, 166, 493-502.
(15) Ma, F. D.; Jin, Y. M.; Wang, Y. U.; Kampe, S. L.; Dong, S. Phase Field Modeling and Simulation of Particulate Magnetoelectric Composites: Effects of Connectivity, Conductivity, Poling and Bias Field. *Acta Mater.* **2014**, 70, 45-55.
(16) Huang, Y. Y.; Jin, Y. M. Phase Field Modeling of Magnetization Processes in Growth Twinned Terfenol-D Crystals. *Appl. Phys. Lett.* **2008**, 93, 142504-142506.
(17) Wang, Y. U. Field-Induced Inter-Ferroelectric Phase Transformations and Domain Mechanisms in High-Strain Piezoelectric Materials: Insights from Phase Field Modeling and Simulation. *J. Mater. Sci.* **2009**, 44, 5225.
(18) Geng, L. D.; Yan, Y.; Priya, S.; Wang, Y. U. Theoretical Model and Computer Simulation of Metglas/PZT Magnetoelectric Composites for Voltage Tunable Inductor Applications. *Acta Mater.* **2017**, 140, 97-106.
(19) Hubert, A.; Schäfer, R. *Magnetic Domains: The Analysis of Magnetic Microstructures*, first ed.; Springer-Verlag Berlin Heidelberg: 1998.
(20) Amin, A.; Haun, M. J.; Badger, B.; McKinstry, H.; Cross, L. E. A Phenomenological Gibbs Function for the Single Cell Region of the $PbZrO_3$:$PbTiO_3$ Solid Solution System. *Ferroelectrics* **1985**, 65, 107-130.

(21) Jin, Y. M. Phase Field Modeling of Current Density Distribution and Effective Electrical Conductivity in Complex Microstructures. *Appl. Phys. Lett.* **2013**, 103, 021906-021909.
(22) Haun, M. J.; Zhuang, Z. Q.; Furman, E.; Jang, S. J.; Cross, L. E. Electrostrictive Properties of the Lead Zirconate Titanate Solid-Solution System. *J. Am. Ceram. Soc.* **1989**, 72, 1140-1144.
(23) Snelling, E. C.; Giles, A. D. *Ferrites for Inductors and Transformers*, first ed.; Research Studies Press: New York, 1983.
(24) Nakano, A.; Aoki, T.; Kimura, O. Control of Thermal Expansion Coefficient of Low Temperature Sintering Ferrites. *J. Jpn. Soc. Powder Powder Metall.* **2002**, 49, 661-665.
(25) Murthy, S. R. Thermal Variation of Elastic Modulus on Nanocrystalline NiCuZn Ferrites. *J. Ceram.* **2013**, 2013, 451863-451869.
(26) Cook, W. R.; Berlincourt, D. A.; Scholz, F. J. Thermal Expansion and Pyroelectricity in Lead Titanate Zirconate and Barium Titanate. *J. Appl. Phys.* **1963**, 34, 1392-1398.
(27) Biswas, D. R.; Chandratreya, S.; Pask, J. A. Thermal Expansion, Elasticity, and Internal Friction of Polycrystalline PZT Ceramic. *Am. Ceram. Soc. Bull.* **1979**, 58, 792-794.
(28) Smit, J.; Wijn, H. P. J. *Ferrites*, Philips' Technical Library: Netherlands, 1959.
(29) Visser, E. G. *Magnetization Processes in Stressed Monocrystalline Manganese Zinc Ferrite*. Doctor of Philosophy Technische Hogeschool Eindhoven, 1983.

For Table of Contents Only (Abstract Graphic)